Experiments in Fluids 31 (2001) 664–673 © Springer-Verlag 2001

Cavity and flow measurements of reproducible bubble entrainment following drop impacts

P. A. Elmore, G. L. Chahine, H. N. Oguz

Abstract High-speed motion pictures of air–water interface dynamics of drop impacts that reproducibly make bubbles are presented. The pictures show previously unobserved details of the phenomenon. Measurements are compared with available computational methods. Experimental and numerical results agree with each other on the overall shape of the interface and the occurrence of bubble detachment. Measurements, however, show that the cavity depth stagnates before bubble entrapment. This behavior is not predicted by simulation. Also discussed are the presence of a jet that strikes the new bubble after formation and the possible effect of droplet surface oscillations on bubble entrainment.

1
Introduction

Regular entrainment, first detected by Pumphrey and Crum (1988), occurs when a bubble is generated reproducibly by a single water drop striking a free surface of a pool of water (Fig. 1). When the surface tension of the liquid in the drop and the larger body of water is 74 dynes/cm, the process occurs when the drop has a diameter and impact velocity within the domain shown in Fig. 2. Studies by Prosperetti et al. (1989), Pumphrey et al. (1989), Pumphrey and Crum (1990), Medwin et al. (1990), Pumphrey and Elmore (1990), Chahine et al. (1991) and Prosperetti and Oguz (1993) show that the dynamics of regular entrainment in tap water are as follows. A drop strikes a large body of water at rest. After impact, a crater forms. As the interface moves back to its initial position, the sides of the crater close on themselves, leading to the bottom part of the cavity separating from the rest of the interface and becoming a bubble. The bubble emits sound and is left behind the rest of the cavity as the interface recedes to the original free surface position.

Most of the analysis of such experiments concentrates on the acoustics related to the event rather than on the dynamics of the interface. These investigations have, however, found some mechanics that are worth noting: (a) as the drops get smaller, the impact velocity required for regular entrainment increases and the generated bubble gets smaller; (b) the bubble size is most reproducible when the drop strikes the water at a speed between its upper and lower impact velocity limits (Fig. 3); (c) the dependence on surface tension is noticeable (e.g., the same drop that strikes a body of water that has a surface tension of 74 dynes/cm and creates a bubble by regular entrainment does not produce a bubble when the surface tension is lowered to 30 dynes/cm); (d) the shape of the crater at its maximum volume changes with impact velocity: at lower speeds, the cavity is conical; as the speed increases, it becomes more hemispherical.

Oguz and Prosperetti (1990) have numerically simulated the dynamics of the interface and the resulting bubble creation just before detachment. They suggest that the bubble is entrapped because the bottom part of the cavity has a downward momentum that is larger than the sides of the cavity and that this momentum is so large that the buoyancy does not reverse the motion before the sidewalls meet. A large downward momentum apparently is sufficient for air entrainment as demonstrated for "bucket-drop" experiments done by Kolani et al. (1994) and entrainment from ice-spheres, as demonstrated by Crum et al. (1992). In these events, the downward momentum is much larger than the momentum parallel to the surface. It is reasonable to suspect that similar mechanics may cause bubble entrainment for single drop impacts. However, this

Received: 25 April 2000 / Accepted: 26 April 2001

P. A. Elmore (✉), G. L. Chahine
Dynaflow Inc., 7210 Pindell School Road
Fulton, MD 20759, USA

H. N. Oguz
Department of Mechanical Engineering
The Johns Hopkins University
Baltimore, MD 21218, USA

P. A. Elmore
National Center for Physical Acoustics
University of Mississippi, University
MS 38677, USA

Present address: P. A. Elmore
Naval Research Laboratory, Marine Geosciences Division
Stennis Space Center, MS 39529, USA

The data for Figs. 2, 3 and 5 and Table 1 were obtained by the first author using the facilities of Dr. L.A. Crum and Dr. H.C. Pumphrey when they and the first author were associated with the National Center for Physical Acoustics at the University of Mississippi. The use of the 16-mm stop-motion projector was provided by Dr. H.E. Bass and Dr. A.R. Kolani at the National Center for Physical Acoustics. The authors thank Drs. Bass, Crum, Kolani and Pumphrey along with Dr. B.C. Denardo, Dr. M.S. Longuet-Higgins, Dr. A. Prosperetti, Mr. S. Gupta, and Ms. K. Wink for their helpful discussions, logistical help, and use of equipment. Funding provided by the Office of Naval Research, Dynaflow, Inc. and the National Center for Physical Acoustics at the University of Mississippi.

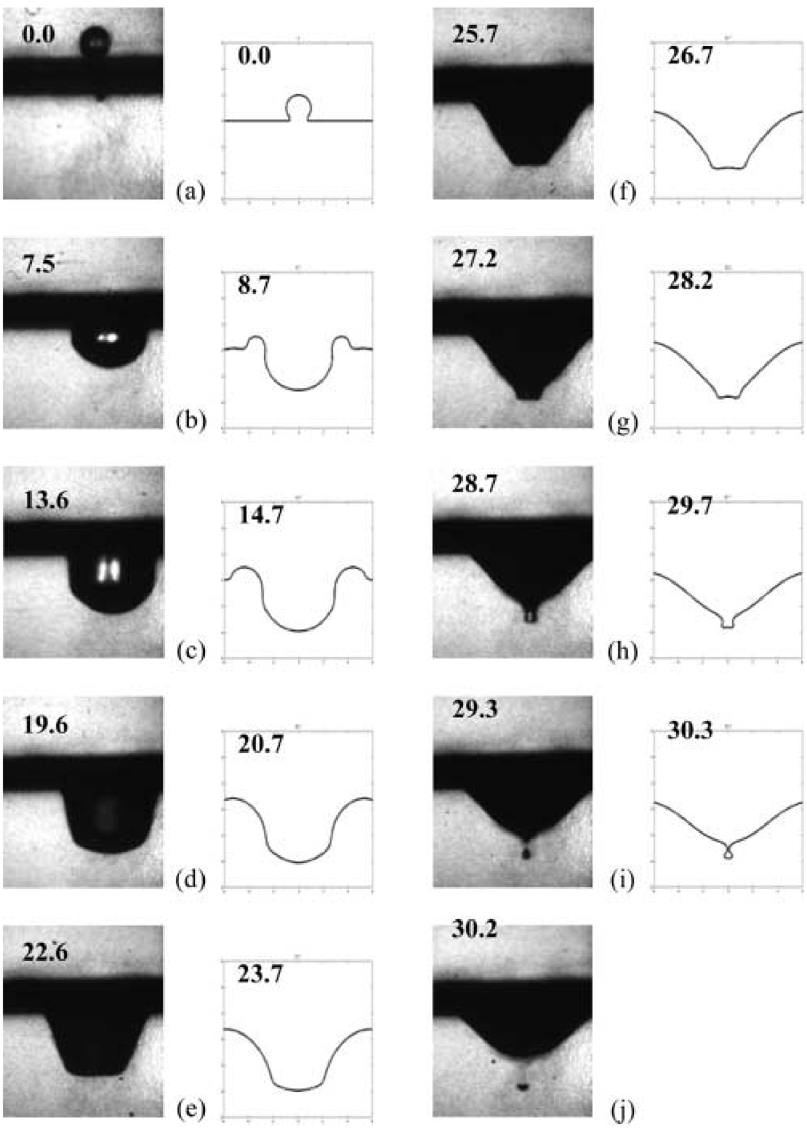

Fig. 1a–j. Experimental results and calculations of regular entrainment from a drop with radius $R = 1.29 \pm 0.03$ mm striking the free surface at a velocity of $U = 1.95 \pm 0.06$ m/s (referred to as "event E1"). The time, t, corresponding to each figure is given in the picture in dimensionless time, $t^* = Ut/R$. Uncertainty in t^*: 0.2

reasoning does not explain why regular entrainment does not occur if one increases the impact speed beyond the upper impact velocity limit of Fig. 2. Theoretical analysis also has been performed by Longuet-Higgins (1990), who studied the fluid flow at the cavity boundary analytically. He proposes that the acoustic emissions from the bubble are a result of the inward flow of fluid at the moment the bubble is formed.

Although regular entrainment has been studied extensively in the laboratory and simulated on the computer, these studies have provided inadequate physical insight for understanding why the bubble is produced. In order to gain further insight, this paper examines the cavity depths for drop impacts, some of which lead to regular entrainment and some do not. Measurements are made from high-speed motion pictures and compared with the predictions obtained from the numerical methods presented in Oguz and Prosperetti (1990). The methods used to obtain these experimental data are presented in Sect. 2. A brief discussion of the numerical calculations is in Sect. 3. The data from these experiments and calculations are shown and analyzed in Sect. 4. Discussion and conclusions are presented in Sects. 5 and 6.

2
Experimental procedures

The dynamics of water drops falling from a hypodermic needle and striking a larger body of fluid at normal incidence are filmed. The setup (Fig. 4) is operated in the following manner. Tap water is put into a rectangular glass tank 25.5 cm long by 25.3 cm wide by 20.3 cm high. The tank is filled to three-fourths capacity with tap water and placed on a lab table. A hypodermic needle is attached to a syringe and suspended over the tank. A HYCAM II 16 mm high-speed film camera equipped with a Canon 70-210 macro lens and extension tubing is placed in front of the tank (the tubing allowed for the longer focal length settings on the lens to be used and increased the magnification). The camera is loaded with either Ecktar 7277 black and white film or Ektachrome 7250 color film, both made by Kodak. Two 500-W tungsten spot lamps that are behind the tank are turned on. The light illuminates the tank

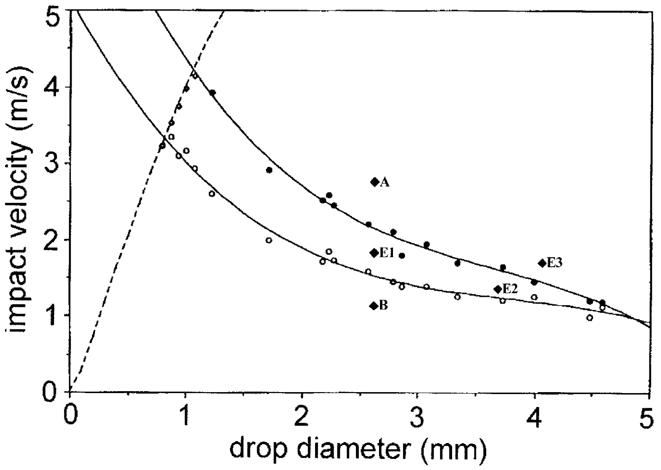

Fig. 2. The domain for which regular entrainment occurs as a function of drop size and impact velocity. The two solid curves are cubic fits of the highest (*solid circles*) and lowest (*open circles*) impact velocities that regular entrainment is observed. The *dotted line* is the terminal velocity curve. Coordinates for the cases filmed in this study, which are listed in Table 1, also are plotted (*diamonds*) and labeled (adapted from Elmore et al. 1989)

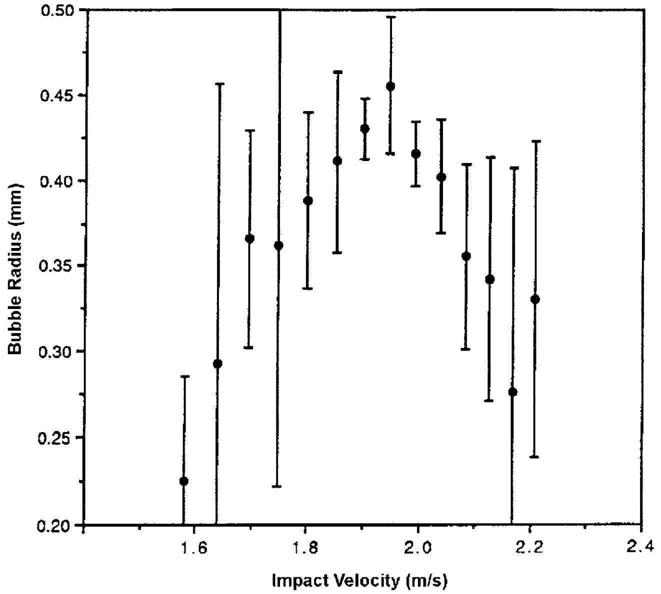

Fig. 3. Bubble sizes for regularly entrained bubbles from a drop 1.29 mm in radius at different impact velocities. Each point is an average of 30 events; the *error bar* is the standard deviation (from Elmore et al. 1989). The graph for bubble frequency vs impact velocity for this case is given in Pumphrey and Elmore (1990)

evenly after passing through a frosted screen. Two similar tungsten lamps also illuminate the tank from the sides.

Tap water dyed with blue food coloring is placed into the syringe. The drops are dyed so that drop fluid is distinguishable from the fluid in the tank; clear drops also are used in some trials for control purposes. Drops are allowed to flow slowly through the needle and fall into the tank. The cavity that forms is viewed through the camera and brought into focus. Drops are then prevented from falling into the tank. The camera speed is set at 5,000 frames/s.

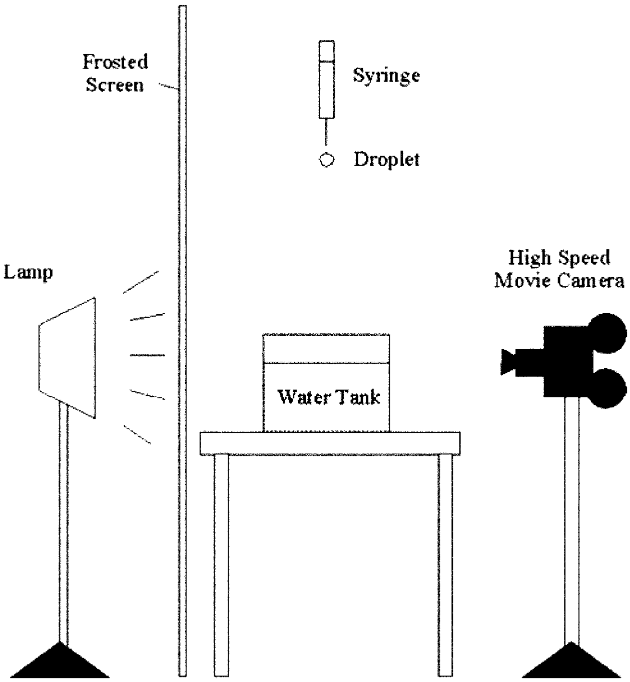

Fig. 4. Diagram of the experimental setup

The water in the tank is gently stirred to diffuse any coloring. After the tank water has settled, the camera is turned on and drops are allowed to strike the water again. The camera then films the dynamics of the impact.

Drop radii are calculated from volume measurements, which are made by capturing the drops on a flat plastic plate and pipetting the water into a microliter syringe. Measurements are made on 30 drops, and average volumes are calculated. The shape of the drops is assumed to be spherical so that an average drop diameter may be calculated.

Drops larger than 2 mm in size are formed by allowing the water to drip from the syringe. The size is controlled by the needle diameter; standard 16, 20, 26, and 30 gauge sizes are used (the inner diameter of the needle decreases in size as the gauge number increases). The ends are sharp. Drops smaller than 2 mm (used only to complete Fig. 2) could not be produced by this method (surface tension adheres the droplet to the needle until the drop accumulates enough weight to overcome this force). A shaker device described in and built by the first author of Pumphrey and Elmore (1990) was used to produce these drops. This device consists of a loudspeaker that is driven by a square wave signal. The needle is attached to the speaker. Water flows through the needle and is jettisoned by the impulse of the speaker. The droplets that are formed have horizontal momentum, but appear to strike the water vertically to a good approximation.

The impact velocity, v_i, was controlled by changing the height of the drop fall, z. The impact velocity is related to the height by the following equation (Pumphrey 1989)

$$v_i = v_t\left[1 - \exp\left(\frac{2gz}{v_t^2}\right)\right]^{1/2}, \tag{1}$$

where v_t is the terminal velocity, and g is the gravitational acceleration. The terminal velocity is known from experimental data of Gunn and Kinser (1949) as published in a paper by Dingle and Lee (1972). Linear interpolation is used to estimate terminal velocities between Gunn and Kinser's data points when needed.

The drop sizes and impact velocities for the events filmed are plotted in Fig. 2 and tabulated in Table 1. The impact events labeled E1 and E2 are expected to produce a single bubble by regular entrainment. The bubble sizes produced by these events also are listed. The sizes are determined by measuring the acoustic frequency of the radiated sound (Fig. 5) with a Brüel and Kjær 8103 hydrophone and a LeCroy 9400 digital oscilloscope. The

Table 1. A listing of the drop diameters, impact velocities and bubble diameters (when applicable) for the events photographed in this study (from Elmore et al. 1989). The events are labeled E1, E2, E3, A and B

Case	Drop diameter (mm)	Impact velocity (m/s)	Bubble diameter (mm)
E1	2.59 ± 0.05	1.95 ± 0.06	0.92 ± 0.08
E2	3.71 ± 0.07	1.45 ± 0.05	0.98 ± 0.04
E3	4.01 ± 0.09	1.75 ± 0.05	Multiple bubbles
A	2.59 ± 0.05	2.70 ± 0.04	No bubble
B	2.59 ± 0.05	1.24 ± 0.04	No bubble

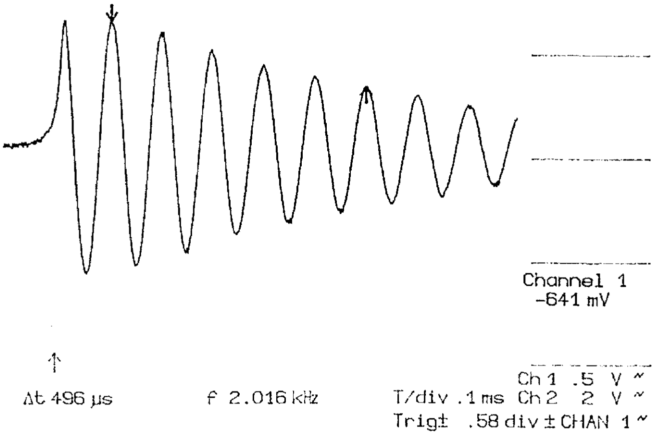

Fig. 5. Acoustic pressure from a regularly entrained bubble. Frequency of oscillation: 10 kHz. Window length: 1 µs (from Elmore et al. 1989)

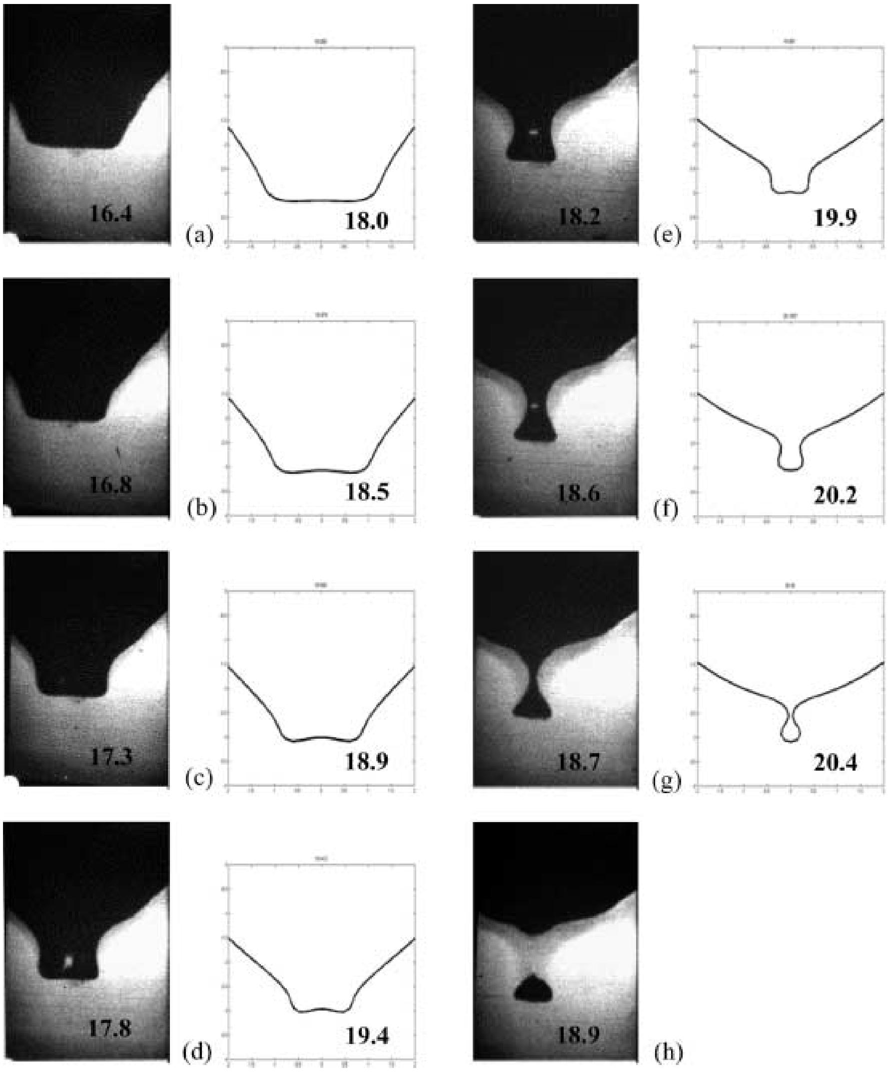

Fig. 6a–h. Close-up pictures and calculations of bubble formation for event E2. The value of t^* for each figure is given in the picture. Uncertainty in t^*: 0.1

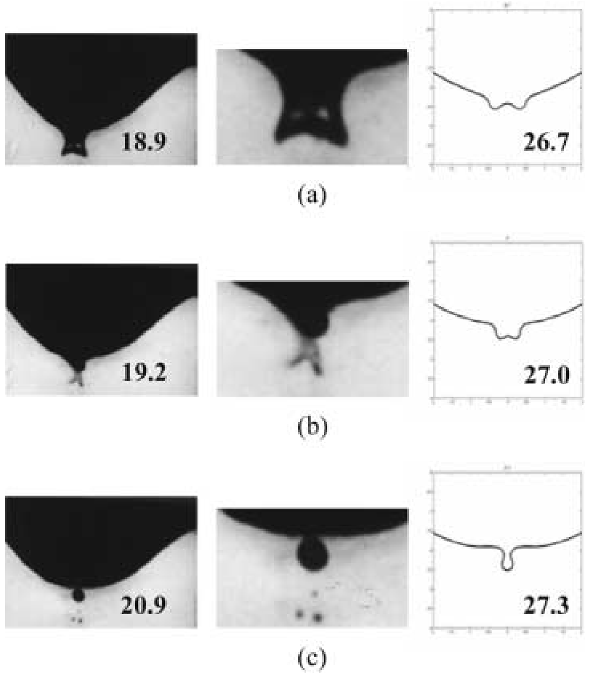

(a)

(b)

(c)

Fig. 7. Pictures and calculations of bubble entrainment for event E3; enlargements of the pinch-off are given in the center of each subfigure. Experiment shows multiple bubbles are formed. The value of t^* for each figure is given in the picture. Uncertainty in t^*: 0.1

radius, r, is calculated from the acoustic frequency by Minneart's equation (Minneart 1933)

$$r^2 = \frac{3\gamma P_o}{\rho_o \omega^2} \quad , \tag{2}$$

where γ is the ratio of specific heats of air, P_o is the ambient pressure, ρ_o is the water density, and ω is the radial frequency (both the entrapped gas pressure and surface tension are neglected in this formula). The acoustic measurements are made in a separate tank that holds approximately one cubic meter of water and was about one meter deep. This larger tank delays reflections from the tank bottom long enough to measure the period of at least ten oscillations. Event E3 is expected to produce a bubble, multiple bubbles, or no bubbles unpredictably from one impact to the next. Events A and B are not expected to produce bubbles because the impact velocities are too high and too low, respectively, for bubble entrainment to occur. (The drop and receiving fluid for cases A and B actually are 10 mmole solutions of potassium phosphate, monobasic and dibasic, respectively. Any effects these compounds have on the overall shape and dynamics of these cavities are assumed to be small.)

Spatial measurements from the motion pictures are obtained by projecting frames of the motion picture on a screen with a 16-mm motion picture projector that has slow motion and freeze-frame capabilities. The depth of the cavity is measured from drop contact to a few frames past the birth of the bubble. For events E1, A and B, the image of the drop is also measured so that the depth measurements may be determined absolutely. For event E2, the bubble is measured instead, since the drop is unseen (drop contact is detectable because of the injection of microbubbles and dyed drop fluid into the receiving liquid immediately after impact and before a cavity begins to form).

Still photographs from the motion picture are made by photographing the projected images with a 35-mm camera when the motion picture projector is in freeze-frame mode. The print pictures are scanned into a personal computer and enhanced with Corel PhotoHouse software.

3
Numerical calculations

The dynamics of the free surface following drop impact were calculated by the boundary integral method described in Oguz and Prosperetti (1990), Zhang et al. (1993), and Chahine (1995). When the drop hits the pool surface, very little vorticity is generated by the impact. During the subsequent development of the cavity, vorticity production at the free surface is minimal in view of the fact that the Reynolds number is of the order of a thousand. Therefore, the flow can be assumed to be irrotational to a good degree of approximation. In this situation, the flow field can be considered to be potential. The application of the Bernoulli integral at the free surface enables one to compute the value of this potential at each time step by integration, in time. The velocity field is then computed by solving the linear system that results from the discretization of Green's identity. The stiffness of the system caused by the inclusion of surface tension effects, but not viscosity, forced us to employ smoothing techniques described in Oguz and Prosperetti (1990). In addition, cubic spline accuracy is achieved for the known quantities of the surface as well as the unknowns by an iterative procedure. The calculations were made using the same drop sizes and impact velocities from the experiment, and the initial shape and flow conditions were specified in the same way as in Oguz and Prosperetti (1990). The output of the calculation gave the radius and depths of discrete points along the interface at each time step. These results were read into MATLAB scripts that plotted the calculated cavity profile, the depth of the point along the symmetry axis, and the depth of the deepest point of the cavity (which may be off-axis). The calculated width of the channel between the birthing bubble and the rest of the cavity also is graphed. The points are joined together with straight lines to produce the curves. The cavity profiles are actually produced by calculating cubic splines between the points as noted above; however, since a large number of points are calculated at each time step, straight lines are used for plotting purposes.

4
Results

The behavior of the interface was filmed successfully at 5,000 frames/s as a drop struck the surface perpendicularly (4,200 frames/s for one event for case E1). Frames from these movies are shown for cases E1, E2, E3, B, and A in Figs. 1, 6, 7, 8, and 9; the calculations of the interface corresponding to the events are shown next to the pictures. The time index for each picture and calculation is

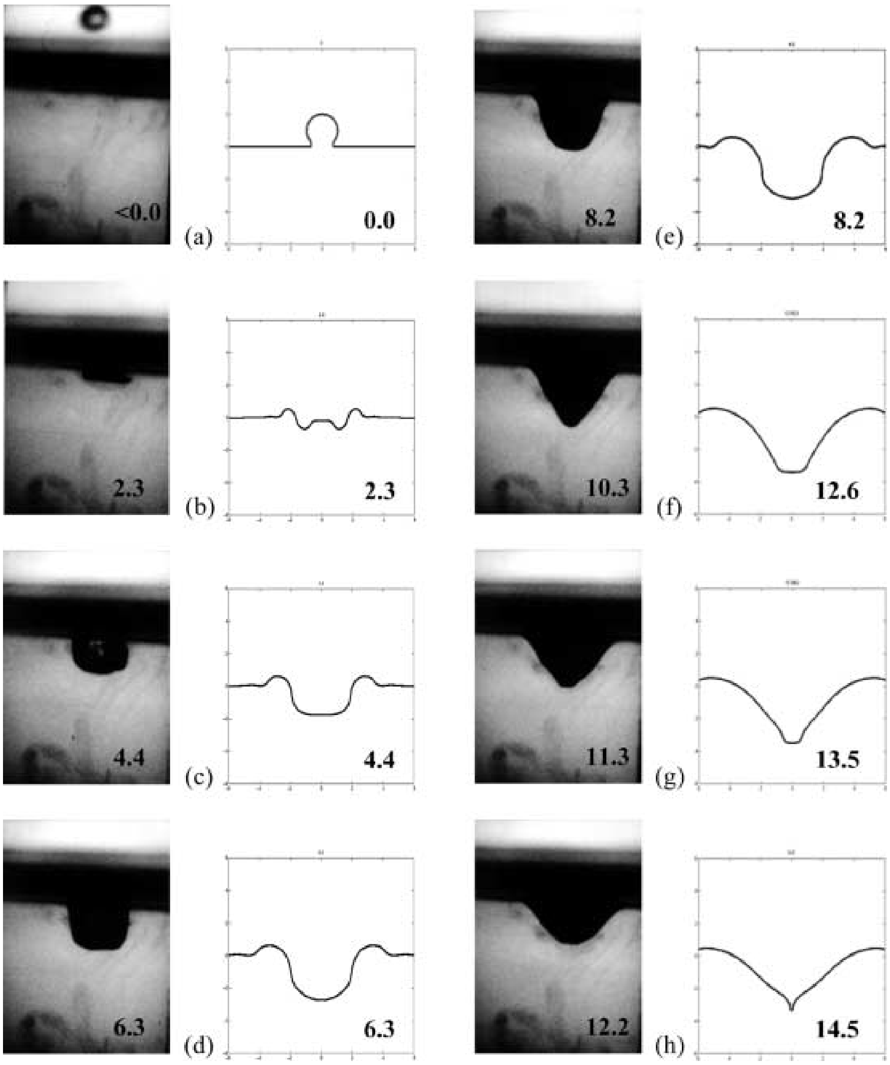

Fig. 8a–h. Drop impact case B. The value of t^* for each figure is given in the picture. Uncertainty in t^*: 0.2

given in dimensionless time, $t^* = Ut/R$, where U is the impact velocity and R is the drop radius.

In the still pictures, the opaque part beneath the interface is the cavity itself. Dye from the drop is translucent and distinguishable from the host fluid, lining the outer boundary of the cavity. A bubble is formed by regular entrainment for cases E1 (Fig. 1) and E2 (Fig. 6). Similar sized bubbles and cavity depths form when the drops are dyed or clear. For case E3 (Fig. 7), bubbles may be absent or may form as the cavity closes; it was not possible to predict bubble production from one drop to the next during the experiment for this case. The numerical computations, however, predict a bubble is produced. The observed depth for cases E1, E2, A, and B are plotted as functions of dimensionless time in Figs. 10–12 in units of dimensionless depth, $z^* = z/R$, where z is the depth. This depth may be off-axis during some of the evolution of the cavity (as shown, for example, in the theoretical calculations in Fig. 6a–d), but is the only measurable depth due to opaqueness of the cavity. Also shown are two theoretical curves; the solid curve plots the visible depth of the cavity and the dashed curve plots the depth of the point along the axis of symmetry. Figure 11 has more resolution than Fig. 10 because the magnification for case E2 is greater than the magnification for E1.

The total experimental uncertainty for an event is given in the appropriate figure caption. The uncertainties for the spatial measurements measured from the projections of the motion picture on the wall is less than 1% for all cases. When these measurements are scaled into dimensionless units, however, the propagation of the errors in the parameters needed for dimensionless scaling increases the uncertainty.

When the drop makes contact with the water (Fig. 1a), drop fluid enters the water before the cavity forms. Drop fluid lines the outer boundary of the cavity at the bottom and sides as the crater grows both in depth and width (Fig. 1b, c). As the crater develops, a capillary wave is observed to travel down the side of the crater to the bottom. When the wave reaches the bottom, it forms a downward peak (the moment when the capillary wave reaches the bottom of the crater corresponds to the small peak at $t^* = 10$ seen in Fig. 11a, b). At this point, the crater is at its greatest depth before the bubble detachment process begins. Eventually, the peak subsides, and the walls become vertical so that the crater has a cylindrical shape with a rounded bottom (Fig. 1d).

The walls then cease to be vertical and form an angle with the axis of symmetry (Fig. 1e). The crater shape evolves from a cylindrical shape with a rounded bottom to

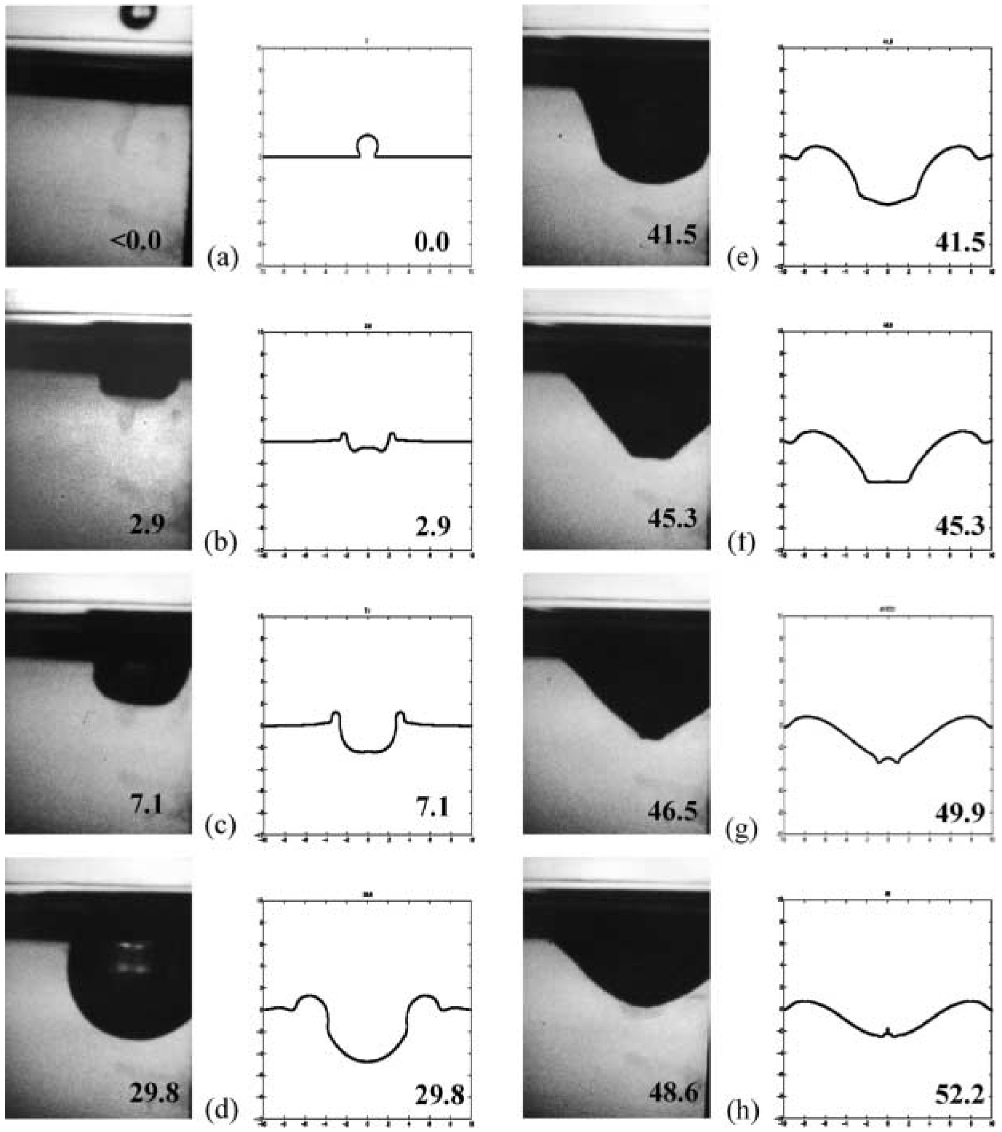

Fig. 9a–h. Drop impact case A. The value of t^* for each figure is given in the picture. Uncertainty in t^*: 0.1

a cone with a flat bottom (Figs. 1f, 6a). The microbubbles located at the bottom of the cavity appear to move slightly upward along the axis of symmetry, indicating that the interface along the symmetry axis is convex and that the deepest points of the cavity are now off-axis. At this point, an axisymmetric inward flow of fluid normal to the symmetry axis develops outside the cavity just above the crater floor (Figs. 1g–h, 6b–d) and the upward axial flow appears to stagnate. Flow into the constriction from the host fluid is apparent because the dye from the droplet stays in contact with the interface as the channel that connects the birthing bubble with the rest of the crater decreases in width (Fig. 6e–g). The crater now resembles a cone with a nipple-like protrusion at its bottom. The protrusion moves deeper into the water as the channel narrows (Figs. 10, 11) and is then disconnected from the rest of the crater when opposite sides of the channel connect (Figs. 1i, 6g). This disconnected part becomes the bubble (Fig. 6h). The dimensionless diameter of the channel between the cavity and birthing bubble, $d^* = d/Z$, where d is channel diameter; is shown in Fig. 13 as a function of dimensionless time. Both experimental measurements and theoretical calculations are given. Since there is variability in the time between drop impact and bubble formation, Fig. 13 shows the data and theoretical curve cued to the moment of detachment to get more useful insight as to how the data and computational results compare with each other.

Since the flow of water along the birthing bubble channel is inward and axisymmetric, the only place for the water to go is either up or down and should do both to conserve total momentum at the point of detachment, as discussed in Longuet-Higgins et al. (1991). Therefore, upward- and downward-moving jets should exist. The upward jet is seen at the water initial free surface. Evidence for the existence of the downward-moving jet is shown in Fig. 14. The top of the bubble is flat, and the dye from the drop goes into the bubble in a funnel-shaped flow.

When bubbles are produced for case E3, the crater dynamics appear similar to that of cases E1 and E2 until entrapment begins. At this point, the part of the cavity that is going to be the bubble is not flattened on the bottom but

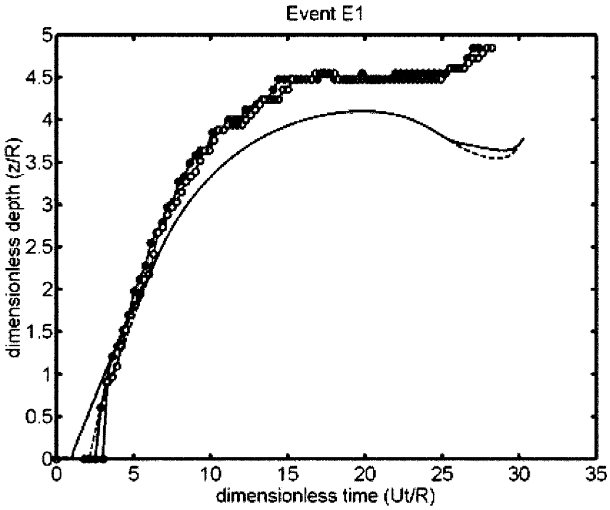

Fig. 10. Crater depth vs time for event E1 with time and depth in dimensionless units. Two measurements of the event are given: E1_1 (*solid circles*) and E1_2 (*open circles*). The visible depth of the cavity as predicted by numerical simulation is given by the *solid curve*; the depth along the symmetry axis as predicted by numerical simulation is given by the *dashed curve*. Uncertainty in t^*: 0.2. Uncertainty in z^*: 4.4% of z^*

curved upward (Fig. 7a). The bubble birth occurs, however, before the floor can rise above the pinch-off point (Fig. 7b). As a result, several bubbles are produced (Fig. 7c).

5
Discussion

An examination of the plots of observable cavity depth vs time for regular entrainment (Figs. 10, 11) shows that the depth stagnates before pinch-off. This stagnation does not appear for events not producing bubbles (events A and B, Fig. 12). For regular entrainment, the experimental measurements disagree with the calculations, which predict a very short-lived reversal in the cavity depth just before bubble birth. The current experimental observations, along with Pumphrey and Crum's (1988) observation that bubble births are nullified when the surface tension is lowered from 75 dynes/cm to 30 dynes/cm suggest that surface tension may be the force competing with buoyancy and trapping the very bottom part of the cavity from rising back to its rest position. Observation of the high-speed pictures seems to indicate that the surface tension force should be the most influential when the cavity takes on a conical funnel shape. Then a small-radius corner is formed at the intersection between the funnel-shaped walls and the bottom of the cavity. Since the deepest parts of the cavity will not move, the restitution of the interface back to its rest position continues along other points where there is less curvature. These points are just above the bottom of the cavity. Fluid flows through these points, moving toward the axis of symmetry until the opposite sides touch. It is this corner that resists disappearance while gravity forces are acting on the interface to bring it back to its original position. When the surface tension is lowered, this radius becomes larger, bringing the configuration closer to an elongated hemispherical shape with less resistance to the restoring force of gravity. In this case, the cavity closes from all sides, and no bubble is formed.

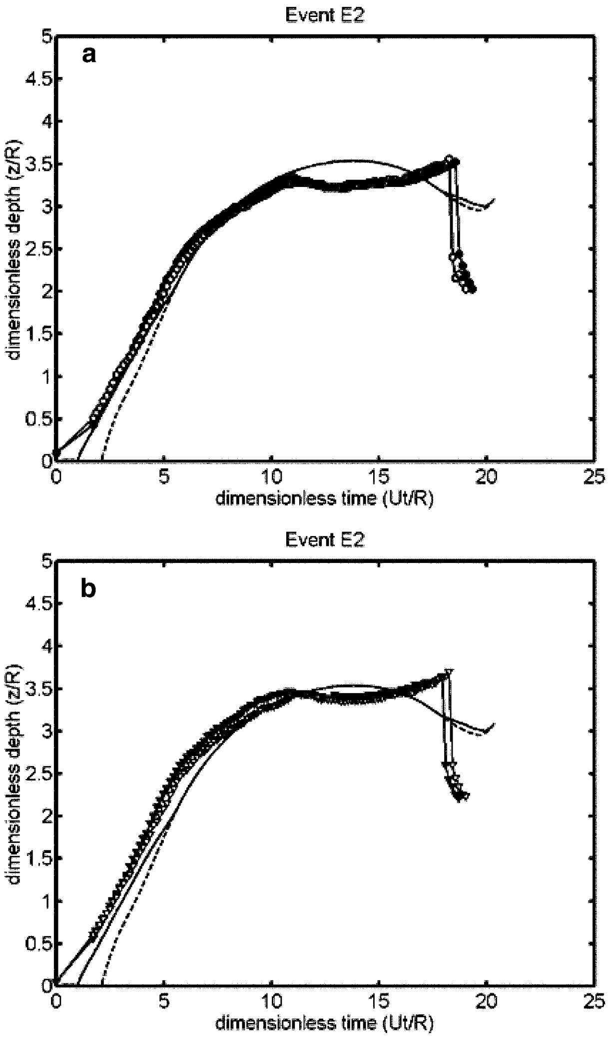

Fig. 11a, b. Crater depth vs time for event E2 with time and depth in dimensionless units. Four trials are measured. Two are given in **a**: E2_1 (*solid circles*) and E2_2 (*open circles*). Two are given in **b**: E2_3 (*solid triangles*) and E2_4 (*open triangles*). The visible depth of the cavity as predicted by numerical simulation is given by the *solid curve*; the depth along the symmetry axis as predicted by numerical simulation is given by the *dashed curve*. Uncertainty in t^*: 0.1. Uncertainty in z^*: 3.6% of z^*

These dynamics also seem to cause the increase in cavity depth observed in Figs. 10 and 11 as the cavity is being separated from the interface. If the cavity bottom stays at a constant depth as the bubble is being formed, the curvature of the channel between the bubble and the rest of the cavity should increase, thereby increasing the surface tension. In order to keep the counterbalance between the surface tension and buoyancy, the curvature cannot increase significantly and consequently the cavity bottom is pushed farther down into the fluid.

As of this point, the droplet has been assumed to be spherical when it strikes the water. When the droplet has surface oscillations, Rodriguez and Mesler (1988) have

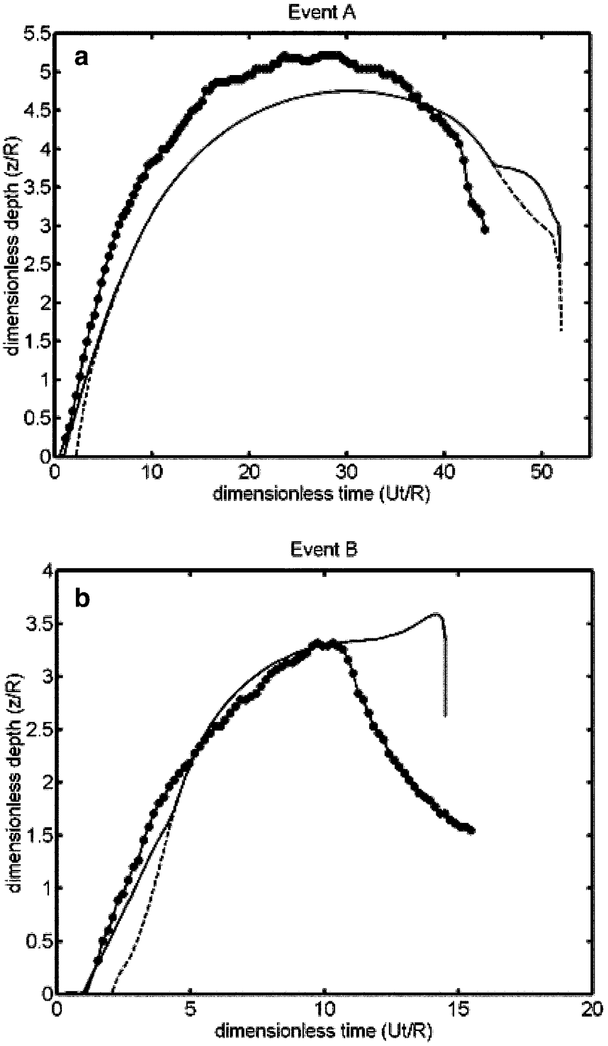

Fig. 12a, b. Crater depth vs time with time and depth in dimensionless units: **a** for case A; **b** for case B. Measurements are indicated by the data points. The visible depth of the cavity as predicted by numerical simulation is given by the *solid curve*; the depth along the symmetry axis as predicted by numerical simulation is given by the *dashed curve*. Uncertainty in t^*: case A 0.2; case B 0.1. Uncertainty in z^*: case A 6.3% of z^*; case B 14.4% of z^*

shown that the shape of the drop at impact affects the width and depth of the cavity produced. A drop that strikes the surface prolate penetrates farther into the water and produces less horizontal momentum as compared with a drop that strikes the surface oblate. For the present experiment, these observations may explain why bubbles are observed for only some E3 impacts while other E3 impacts produce no bubbles; when the drop strikes the surface prolate, the floor can advance far enough into the fluid for the walls to collapse behind it and entrain air. When the drop strikes the surface oblate, then the downward penetration is reduced, and the amount of horizontal spreading increases. In this second case, the floor does not go far into the fluid before reversing direction and does so long before the collapse of the cavity wall could entrain air.

Differences between the numerical results and the experimental observations can also be imputed to the liquid surface tension. Indeed, as mentioned earlier, inclusion of the surface tension effects requires use of smoothing techniques that appear here to affect the results in some detailed aspects without affecting the overall dynamics of the simulated phenomenon.

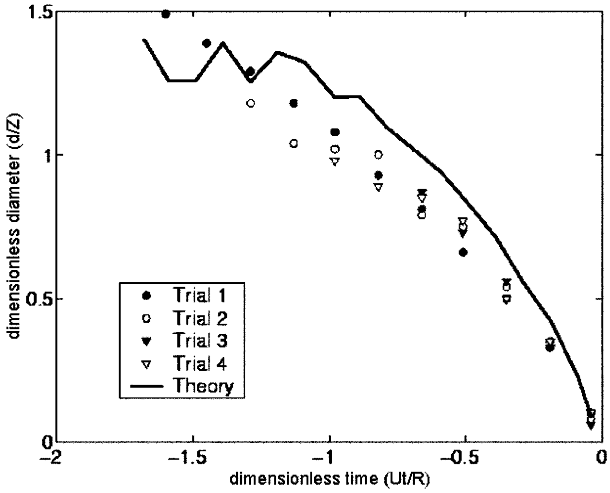

Fig. 13. Diameter of the channel between the cavity and birthing bubble as a function of dimensionless time for event E2. The diameter is given in dimensionless units. The data points are given for the four trials. Results from numerical simulation are given by the *solid curve*. The data points and simulation curve are artificially forced to be zero at time zero in order to make useful comparisons; in actuality, all five sets go to zero diameter at different times relative to the instant of drop impact. Uncertainty in t^*: 0.1. Uncertainty in diameter: 3.6% of the value

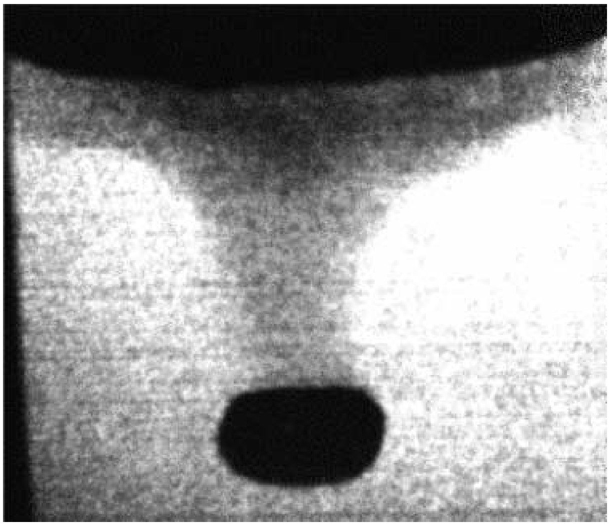

Fig. 14. Downward jet striking the newly formed bubble. Dye is from the drop fluid. Picture taken 0.6 ± 0.1 ms after pinch-off

6
Conclusions

A new set of high-speed motion pictures of regular entrainment was made. Motion pictures were also made of bubble entrapment outside the regular entrainment domain; some impacts produce bubbles while others do not. In these films, the cavity and the detachment of any produced bubbles are magnified, and drop fluid is dyed. Qualitatively, the experimental results and numerical simulations are in agreement; however, a disagreement is noted quantitatively. Analysis of these films shows that the depth of the cavity stagnates for much of the cavity life before a bubble is formed by regular entrainment. These measurements are not reproduced by the current numerical simulations, which predict a much shorter reversal of cavity depth just before detachment. The discrepancy may be due to surface tension-forced smoothing or to the neglect of vorticity, which underestimates the downward momentum of the crater. The stagnation is absent in both experiment and simulation when the impact does not lead to bubble production.

The experimental observations suggest that surface tension may counterbalance buoyancy exerted on the floor of the cavity before bubble entrapment. As a result of the bottom of the cavity not moving, the collapse of the cavity continues along other parts of the interface with water flowing axisymmetrically to a point above the cavity floor.

Other observations also are noted, such as the presence of a downward jet that pushes downward into the newly formed bubble as seen from the dyed drop fluid. In addition, the phase of the surface oscillation of the drop may govern the production of bubbles, with entrainment being most likely when the drop strikes the surface prolate.

References

Chahine GL (1995) Bubble interactions with vortices. In: Green S (ed) Vortex flows, Chap. 18. Kluwer Academic, Dordrecht

Chahine GL, Wink K, Gupta S, Elmore PA (1991) Bubble formation following drop impact at a free surface. In: Furuya O, Kato H (eds) Cavitation and multiphase flow forum: FED vol 109. ASME, New York, pp 63–68

Crum LA, Roy RA, Prosperetti A (1992) The underwater sounds of precipitation. Naval Res Rev 2: 2–12

Dingle NA, Lee Y (1972) Terminal fallspeeds of raindrops. J Appl Met 11: 877–879

Elmore PA, Pumphrey HC, Crum LA (1989) Further studies of the underwater noise produced by rainfall. Tech Report, National Center for Physical Acoustics – University of Mississippi, NCPA LC.02.89

Gunn R, Kinser GD (1949) The terminal velocity of fall for water droplets in stagnant air. J Met 6: 243

Kolani AR, Roy RA, Gardner DL (1994) Low-frequency acoustic emissions in fresh and salt water. J Acoust Soc Am 96: 1766–1772

Longuet-Higgins MS (1990) An analytic model of sound production by raindrops. J Fluid Mech 214: 395–410

Longuet-Higgins MS, Kerman BR, Lunde K (1991) The release of air bubbles from an underwater nozzle. J Fluid Mech 230: 365–390

Medwin H, Kurgan A, Nystuen JA (1990) Impact and bubble sound from raindrops at normal and oblique incidence. J Acoust Soc Am 88: 413–418

Minneart M (1933) On musical air bubbles and the sounds of running water. Phil Mag 16: 235–248

Oguz HN, Prosperetti A (1990) Bubble entrainment by the impact of drops on liquid surfaces. J Fluid Mech 219: 143–179

Prosperetti A, Oguz HN (1993) The impact of drops on liquid surfaces and the underwater noise of rain. Annu Rev Fluid Mech 25: 1–31

Prosperetti A, Crum LA, Pumphrey HC (1989) The underwater noise of rain. J Geophy Res 94(C3): 3255–3259

Pumphrey HC (1989) Sources of ambient noise in the ocean: an experimental investigation. PhD Dissertation, University of Mississippi

Pumphrey HC, Crum LA (1988) Acoustic emissions associated with drop impacts. In: Kerman BR (ed) Sea surface sound. Kluwer, Norwell, Mass., 463–483

Pumphrey HC, Crum LA (1990) Free oscillations of near-surface bubbles as a source of the underwater noise of rain. J Acoust Soc Am 87: 142–148

Pumphrey HC, Elmore PA (1990) The entrainment of bubbles by drop impacts. J Fluid Mech 220: 539–567

Pumphrey HC, Crum LA, Bjørnø L (1989) Underwater sound produced by individual drop impacts and rainfall. J Acoust Soc Am 85: 1518–1526

Rodriguez F, Mesler R (1988) The penetration of drop-formed vortex rings into pools of liquid. J Colloid Interface Sci 121: 121–129

Zhang S, Duncan J, Chahine GL (1993) The final stage of the collapse of a cavitation bubble near a rigid wall. J Fluid Mech 257: 147–181